Optimization of austenitic and ferritic steels for deep drawing. Part 2: FEM analyses with damage development.

Andrea Casaroli, Edoardo Scabini, Marco V. Boniardi
Department of Mechanical Engineering, Politecnico di Milano, via La Masa 1, 20156 Milano, Italy
andrea.casaroli@polimi.it, https://orcid.org/0000-0001-5207-5547
edoardo.scabini@polimi.it, https://orcid.org/0009-0005-4487-912X
marco.boniardi@polimi.it, https://orcid.org/0000-0002-2438-7890

Riccardo Andreotti
Callens® AREA3, Via Merini 37 21100 Varese, Italy
riccardo.andreotti@callens.it, https://orcid.org/0000-0003-2472-9448

Barbara Rivolta
Department of Mechanical Engineering, Politecnico di Milano, via La Masa 1, 20156 Milano, Italy
barbara.rivolta@polimi.it, https://orcid.org/0000-0002-8949-0549

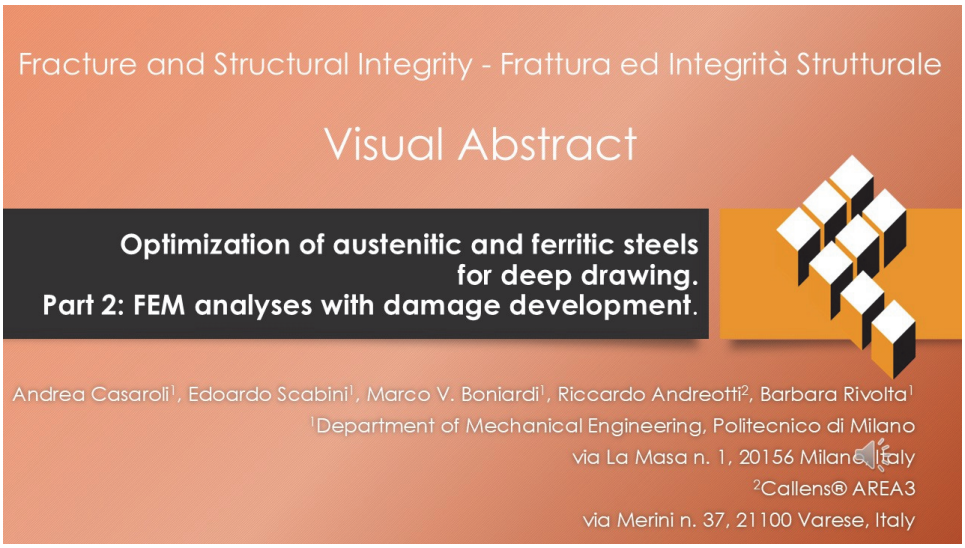

KEYWORDS. Deep Drawing, Stainless steels, FEM analyses, Erichsen test, ANOVA, Process parameters, Lubrication analyses.

OPEN ACCESS

Citation: Casaroli, A., Scabini, E., boniardi, M. V., Andreotti, R., Rivolta, B., Optimization of austenitic and ferritic steels for deep drawing.Part 2: FEM analyses with damage development., Fracture and Structural Integrity, 75 (2026) 179-199.

Received: 05.10.2025
Accepted: 25.10.2025
Published: 25.10.2025
Issue: 01.2026

INTRODUCTION

Deep drawing of stainless steel sheet metal is one of the most widespread technologies in modern industry. The variety of geometries that can be obtained, together with the reduced times and low production costs, make deep drawing the best choice for the production of large quantities of highly corrosion-resistant sheet metal components, an essential requirement for the food industry, for nautical equipment or for the chemical and petrochemical sectors. This technology is also used in the creation of design objects and in high added value solutions in the civil and industrial sectors. Despite its apparent simplicity, the deep drawing process of stainless steel is characterized by a significant technical complexity, due both to the material properties and to the processing parameters which, if not properly controlled, can give rise to defects such as wrinkles, scratches or even component breakage [1]. Improving the process requires an intervention on the operating variables, such as the blank holder force, the deformation rate and the lubrication type, which influence the material's ability to obtain the desired defect-free geometry [2]. Lubrication, which can be achieved using films or liquid lubricants of different nature, plays a crucial role in deep drawing process. First, it significantly contributes to the reduction of tool wear, one of the most relevant problems in this sector. This damage is mainly due to adhesive wear phenomena, which cause the formation of scratches and grooves on the surface of the dies, resulting in a progressive loss of geometric and dimensional tolerances. This type of wear is strictly related to the friction coefficient between the die and the sheet metal: a high friction intensifies the adhesion phenomena, accelerating the tool failure. Second, good lubrication allows the relative motion of the material with respect to the punch, allowing a more homogeneous distribution of stresses and deformations within the sheet metal [3]. Finally, it contributes to increasing the overall efficiency of the process, reducing the forces required for stamping and, consequently, the energy used and the overall mechanical wear of the machinery. One of the central problems in lubrication is related to ensure the permanence of the liquid lubricant between the die and the sheet metal during the deformation phases. The nature of the process involves relative movements between the contacting surfaces, generating shear forces that drag the lubricant out of the working area. This phenomenon causes a progressive reduction in the thickness of the lubricating film, which in critical conditions can be completely removed, giving rise to direct contact between the surfaces. The geometry of the die can further amplify this condition, contributing to the instability of the lubricating film [4]. The prediction of tribological behaviour is also complicated by the other factors at play: the type of lubricant, its viscosity and the variations of its properties induced by temperature and pressure [4]. This combination of variables makes it extremely difficult to model the contact area, forcing to rely on expensive experimental campaigns. The blank holder pressure and the deformation rate also play a significant but less important role than lubrication. In both cases, the process setup must ensure a good compromise between conflicting needs: the pressure must be high enough to avoid the formation of wrinkles without hindering the material flow [5], while the deformation rate must allow to maximize the production without creating problems of sheet metal deformability [6]. From this point of view, it is useful to remember that the deformation rate normally applied in cold forming processes are much lower than those typical of explosions or ballistic impacts ($\dot{\varepsilon} > 100$ 1/s) [7-10], the only ones capable of significantly influencing the mechanical properties of a stainless steel at room temperature. When the geometry of the piece is extremely complex, the number of deformation stages is increased, alternating them with appropriate heat treatments [11], or to optimize the geometry of the product, in order to adapt the process to the stainless steel properties [12]. The most common heat treatments for deep-drawn stainless steels are solution annealing and full annealing. Solution annealing is mainly performed on semi-finished or finished products in austenitic stainless steel. This treatment occurs at high temperatures (usually between 1000°C and 1100°C) for a period of time sufficient to homogenize the chemical composition and solubilize the chromium carbides, improving the corrosion resistance of the steel. To ensure treatment effectiveness, austenitic stainless steels must be rapidly quenched in water to prevent chromium carbide precipitation between 450°C and 900°C. For thin-walled components, a high-pressure nitrogen can also be used. Annealing, applied to ferritic stainless steels, is performed between 770°C and 930°C, depending on the steel's chemical composition. Both the temperature and holding time must be carefully selected to avoid grain growth in ferritic stainless steels. Cooling can be performed differently: thin-walled semi-finished products are cooled in air, while those with a thicker cross-section are cooled in water. Both solution annealing for austenitic stainless steels and full annealing for ferritic ones regenerate the microstructure after cold plastic deformation which, in the case of austenitic stainless steels, can also cause the formation of martensite [13] negatively influencing the quality of the final product. However, the adoption of intermediate heat treatments is not very convenient from the economic point of view, because it increases the production times and requires significant plant modifications. To prevent deformability problems, there are stainless steels specifically designed for deep drawing, which differ from the standard versions in their chemical composition. A significant example is the austenitic stainless steel AISI 304, that has a variant characterized by reduced chromium content and higher level of nickel, in order to reduce the risk of martensite formation during plastic deformation [14]. For ferritic stainless steels, AISI

441 is characterized by a very low carbon content and the addition of small quantities of titanium and niobium that stabilize ferrite and inhibit chromium carbide precipitation. Although these variants are commercially widespread, the performance differences are very limited or, in some cases, completely absent [6]. From this point of view, there are tests, such as the Erichsen test and the Ball Punch Test, designed to systematically analyse the deformability of metal sheets subjected to deep drawing conditions. These methods, defined by the EN ISO 20482 and ASTM E643 standards, aim to simulate the stress conditions of a sheet metal during the deep drawing process. The process uses the movement of a hemispherical punch perpendicular to the surface of a sheet metal clamped by a blank holder. This load causes an increasing plastic deformation up to the fracture point of the steel. The result is the Erichsen index (IE), i.e. the maximum depth of the dome at cracking, which represents a direct indicator of the stainless steel formability under biaxial stress conditions. The Erichsen test allows to quickly obtain an easy-to-read result, which however does not provide any indication on how the sheet metal is deforming as a whole [15]. To answer this question it is useful to remember that to guarantee the volume, the sum of the deformations in the longitudinal, transverse and thickness directions must be equal to zero (1):

$$\varepsilon_l+\varepsilon_w+\varepsilon_t=0 \tag{1}$$

Comparing the in-plane deformations of the sheet metal with those along the thickness, two main categories of deformation can be distinguished (Fig. 1).

- *drawing*: planar deformation is positive in one direction (elongation) and negative in the transverse direction (contraction). This condition is typical of processes in which the material is stretched predominantly in a single direction, with contraction in perpendicular ones. A classic example of this phenomenon is the tensile test, while in the deep drawing process this deformation is created in the sheet metal sliding under the blank holder.
- *stretching*: the deformation on the plane is positive, meaning there is an elongation both longitudinally and transversally. This condition, which is typically observed in the sheet metal in contact with the die, is more critical than in *drawing* because a significant reduction in thickness is required to keep the material's volume constant.

By plotting the in-plane deformations, we can create a graph representing the two deformation modes described above. The bisector of the first quadrant highlights a particular deformation mode, called balanced biaxial, in which planar deformation occurs uniformly in both directions of the plane.

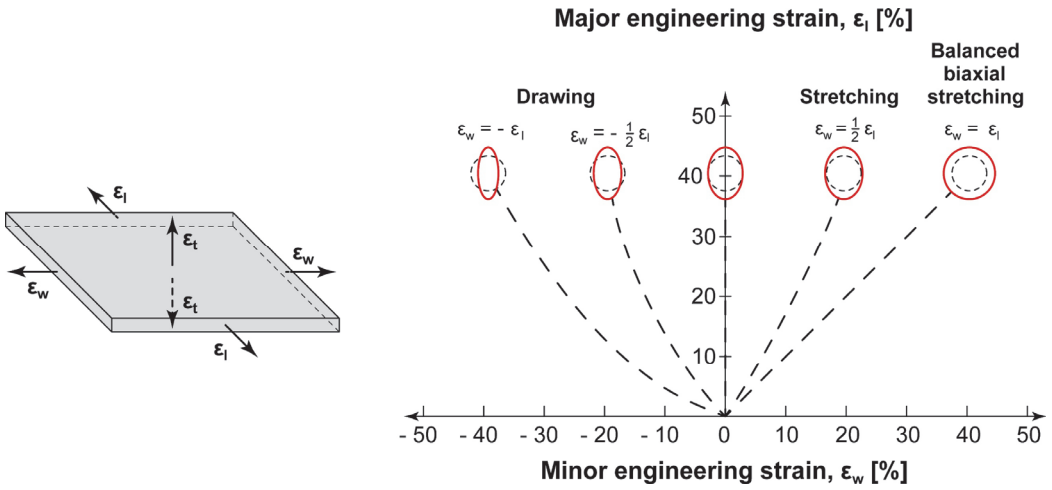

Figure 1: Deformation modes based on planar deformation values. The major and minor deformation are those on sheet metal plane expressed by ε_l and ε_w. In the left area the deformation occurs by drawing while in the right one by stretching.

The same graph can also be used to plot the formability limit curve (Fig. 2) which shows the maximum strain that can be applied before the steel cracks[16]. This curve can be determined in three ways: (i) experimentally, through specific tests, (ii) analytically, using models such as the Storen-Rice one [17] or (iii) numerically, with finite element models.

The formability limit curve is very important in deep drawing processes, as it provides valuable information on the maximum allowable deformation values [18] before the sheet metal breaks. For example, the formability limit curve highlights that the stretching conditions between the punch and the blank holder or the balanced biaxial deformation at the tip of the punch are less critical than the uniaxial ones, which instead block the deformation perpendicular to the force. To fully understand the information provided by the formability limit curves, it is important to evaluate the sheet metal deformation modes to

identify the areas closest to the limit values. A first alternative consists of screen printing a rectangular series of small circles across the whole surface of the sheet metal, measuring the variation in its geometry after the plastic deformation process. This method allows for a precise evaluation of the deformations without, however, providing any indication of their evolution during the forming process. A second limitation is the high costs and testing times, which require the screen printing of all the sheets and the correction of the die geometry for critical issues in the deformation process. A faster and cheaper alternative is the simulation of the deep drawing process by means of finite element models (FEM)[19] potentially able to replace experimental tests with virtual analyses.
When properly calibrated, FEM models highlights stress and strain distribution, identify areas at risk of failure, calculate the final component thickness, and optimize the die geometry. This method discretizes one or more continuous domains (e.g., the sheet metal, the punch, and the blank holder) into a finite set of interconnected subdomains, called "finite elements."

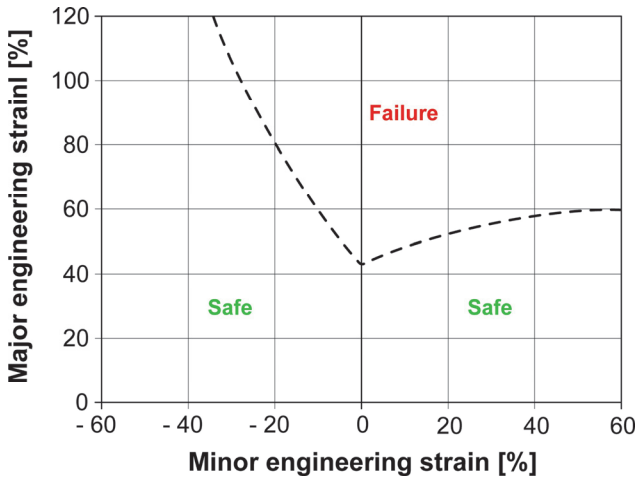

Figure 2: Generical example of a formability limit curve. The image clearly shows how the limit curve for drawing, in the left area, allows larger deformations than the one for stretching, in the right area.

These elements, which can have different geometric shapes (triangles, quadrilaterals, tetrahedra, hexahedrons, etc.), are connected to each other at specific points known as "nodes." The entire network of elements and nodes forms the model's "mesh". Within each element, the material behaviour is approximated by relatively simple mathematical functions, called "shape functions", which describe the deformation and stress in the element as a function of the node displacements. From this perspective, the choice of shape functions is crucial, as it determines the accuracy and convergence of the model. Unlike linear structural analyses, where the objective is to calculate displacements and stresses in the elastic regime, in cold forming processes, such as deep drawing, it is necessary to consider the nonlinear behaviour of steel in its plastic range. Solving nonlinear problems therefore requires an incremental approach in which the deformation process is divided into a series of small time steps. For each step, the software iteratively solves the equilibrium equation $K \cdot \Delta u = \Delta f$, where K is the stiffness matrix, which is updated at each iteration to consider the effect of deformation and steel, while the vectors Δu and Δf represent the increase of displacements and forces [20]. The nonlinear behaviour of steel in the plastic range is instead described through specific constitutive models, such as Hollomon's law (2), which shows the trend of true stresses and strains beyond the yield point.

$$\sigma^{*}=C\times \varepsilon^{*^{n}} \tag{2}$$

where:

- σ^* represents the true stress experienced by the material, calculated as $\sigma^* = \sigma \cdot (\varepsilon+1)$ where σ and ε are the engineering stress and strain, respectively.
- C is the characteristic constant of the material.
- ε^* represent the true strain calculated as $\varepsilon^* = \ln(1 + \varepsilon)$.
- *n* represents the work hardening coefficient, calculated according to ISO 10275.

The Hollomon Eqn. (2) relates the parameters needed to model the plastic behaviour of the material up to the ultimate tensile strength, R_m, and the corresponding percentage plastic extension at maximum force, $A_g\%$ (Fig. 3). Beyond R_m ,

however, the Hollomon equation loses its validity [21] and to obtain the true stress-strain curve from necking to physical fracture of the specimen, different methods can be adopted.
In our case, the problem was solved by comparing the results of the tensile tests used to characterize the stainless steels with the finite element model of the same tests. A grid of 2 mm square elements was printed on the whole surface of the parallel length of the rectangular cross-section tensile specimens, in order to highlight the deformation undergone by these elements during the test. This information allowed to iteratively reconstruct the true stress-strain curve from necking to physical fracture of the tensile specimen, so that the FEM simulation returned the same values observed experimentally [21].

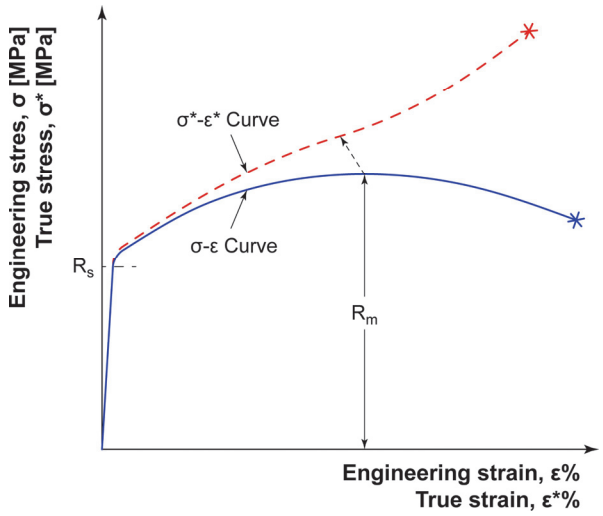

Figure 3: Engineering stress-strain curve (solid blue line) versus true stress-strain curve (dashed red line) for a generic steel.

Another critical aspect, in addition to modelling the true stress-strain curve, is defining the contact between the sheet metal, the punch, and the blank holder. The software must be able to recognize when the mesh nodes of the workpiece come into contact with the tool surfaces and apply the appropriate contact conditions, including friction, which is essential to simulate material flow and stress distribution. This research led to the development of a FEM model dedicated to simulating deep drawing processes under different operating conditions. The model was appropriately calibrated by simulating a series of Erichsen tests on AISI 304 and AISI 430 stainless steel sheets under different lubrication conditions, and then comparing the experimentally in-plane deformations and thickness with the numerically predicted ones. To ensure the accuracy of the true stress-strain curves, both stainless steels were fully characterized through tensile tests, Erichsen tests, and metallographic analyses of the cold-formed samples.

MATERIALS

The experimental activity involved two most commonly industrially used austenitic and ferritic stainless steels, AISI 304 and AISI 430 (ASTM A240), respectively similar to X5CrNi18-10 and X6Cr17 according to the EN 10088 standard. Both steels, produced in 1 mm thick sheets, were supplied in the 2B condition, i.e. annealed, pickled and skin-passed.

[%]	C	Cr	Ni	Mn	Si	S	P	Cu	Mo	N
AISI 304	0.04	18.05	8.02	1.72	0.37	<0.01	0.04	0.04	0.21	0.06
ASTM A240: AISI 304	<0.08	18-20	8-11	<2.00	<0.75	<0.03	<0.045	-	-	<0.10
AISI 430	0.05	16.19	0.55	0.47	0.33	<0.01	0.04	0.04	0.02	0.05
ASTM A240: AISI 430	<0.12	16-18	<0.75	<1.00	<1.00	<0.03	<0.04	-	-	-

Table 1: Chemical composition of the stainless steel sheets used for the experiments compared to the limit values.

TENSILE TEST: REAL TESTS AND FEM SIMULATION

Tensile tests were performed to obtain the mechanical properties of AISI 304 and AISI 430 stainless steels used for the Erichsen tests. For each material, nine proportional tensile specimens were obtained, three parallel (L), three perpendicular (T) and three at 45° (Q) with respect to the rolling direction, in order to verify whether the sheets were homogeneous and isotropic. The tests were performed according to ISO 6892, using a strain rate of 0.005 s^{-1} for the elastic field, then increasing to 0.05 s^{-1} until failure. For each tensile test, the yield strength $R_{p0.2}$, the ultimate tensile strength R_m, the elongation after fracture A% (L_0 = 25 mm), the elongation at maximum load A_g% and the work hardening coefficient, n, calculated according to ISO 10275 in the strain range 4-15% were determined. The results, expressed as the mean value of the three replicates, are reported in Tab. 2.

Material	Direction	$R_{p0.2}$ [MPa]	$R_{p0.2\ -\ avg}$ [MPa]	R_m [MPa]	$R_{m\ -\ avg}$ [MPa]	A%	$A\%_{avg}$	A_g%	$A_g\%_{avg}$	n	n_{avg}
AISI 304	Longitudinal L	270	267	661	650	53	55	47	48	0.343	0.329
	Transverse T	267		646		56		48		0.319	
	45° Q	263		643		56		48		0.324	
AISI 430	Longitudinal L	335	340	487	488	22	21	13	13	0.188	0.177
	Transverse T	343		492		22		13		0.175	
	45° Q	341		484		19		12		0.167	

Table 2: Results of tensile tests (yield strength, $R_{p0.2}$, ultimate tensile strength, R_m, elongation after fracture, A%, plastic extension at maximum force, A_g% and strain-hardening coefficient, n) for the austenitic stainless steels AISI 304 and for the ferritic one AISI 430. The specimens are obtained longitudinal, perpendicular and at 45° respect to the rolling direction and each value is expressed as the mean of three replicates.

The results of the tensile tests (Fig. 4 and Tab. 2) confirm what was expected in the literature [22]: the yield strength of AISI 430 is higher than that of AISI 304 which, however, thanks to its excellent plastic deformability and high work hardening index, shows a higher ultimate tensile strength. The plastic deformability of the C.F.C. lattice, typical of austenitic stainless steels, is in fact higher than that of the C.C.C. lattice. This characteristic is due to the greater distance between the planes of maximum atomic density of the C.F.C. lattice compared to the C.C.C. lattice, compared to which it also has a higher atomic density. Both steels can be considered homogeneous and isotropic, given that the tensile tests have highlighted limited differences along the three different directions.

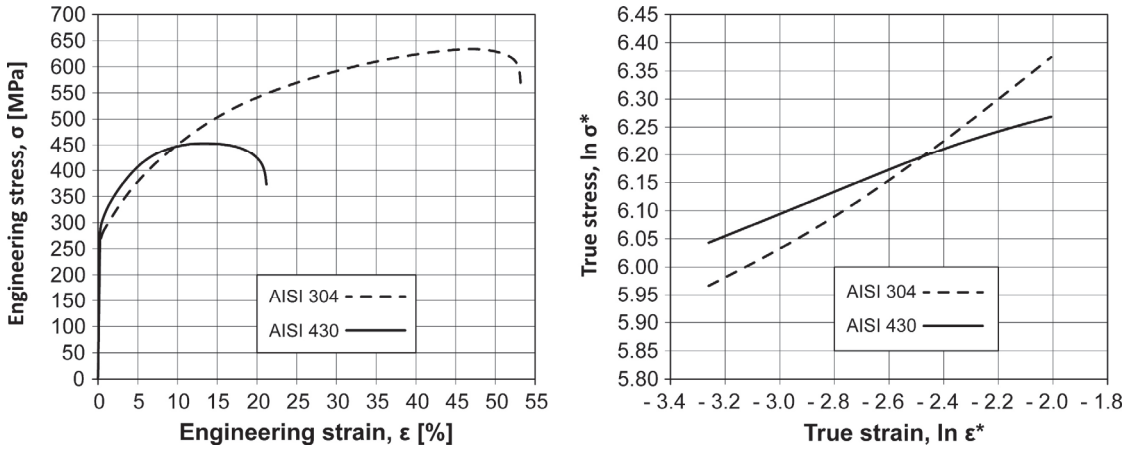

Figure 4: Engineering stress-strain curves (left) and true stress-strain regression lines in the 4%-15% strain range (right) for the austenitic stainless steels AISI 304 and the ferritic stainless steels AISI 430. Both samples are obtained in longitudinal (L) direction.

Simulating an Erichsen test requires a true stress-strain curve describing the behaviour of the steel until physical failure. This problem was solved by comparing the experimental results obtained from the tensile tests with those of a FEM model simulating the same tests. To this end, a grid of 2 mm square elements was printed on the parallel length of the rectangular

cross-section specimens, which allowed the deformation of each element to be measured. It is important to note that up to R_m, the true stress-strain curve was obtained using the average stress and strain data from the tensile tests, appropriately transformed from engineering to true values.

The simulation of the tensile test was performed using the non-linear implicit solver of ABAQUS®/Standard [23]. The geometry of the specimens used for the real tests (Fig. 5-a) was discretized within ABAQUS®/CAE by means of a shell structured mesh scheme (Fig. 5-b) composed of S4R finite elements which are 4-node, quadrilateral, stress/displacement shell element with reduced integration and a large-strain formulation. The size of the elements was set to 1mm. The tensile test simulation applies a gradual relative displacement to the clamped sections of the specimens until the failure happens. Fig. 5-c and Fig. 5-d show that at the end of the simulations, both the geometry and the mesh of the virtual specimens faithfully reproduce the shape of the real specimens and the distribution of the grid printed on the parallel length before the tests. The only significant difference is the position of the fracture area in the virtual model, which lies on a plane at 90° to the specimen axis, rather than at 45° as in the real case. This difference is due to the arbitrary finite elements discretization of the specimens using structured quadrilateral elements of relatively large size (1mm). This choice in fact causes the necking of the specimen to happen in a single plane normal to the axis, driven by the structured mesh instead of the 45° plane of the real case. This approach does not influence the effectiveness of the model in predicting the tensile load and elongation histories (see the load curves validation in Fig. 7) and allows a parsimonious representation of the behaviour of the specimen by minimizing the number of nodes and the overall calculation cost of the simulation.

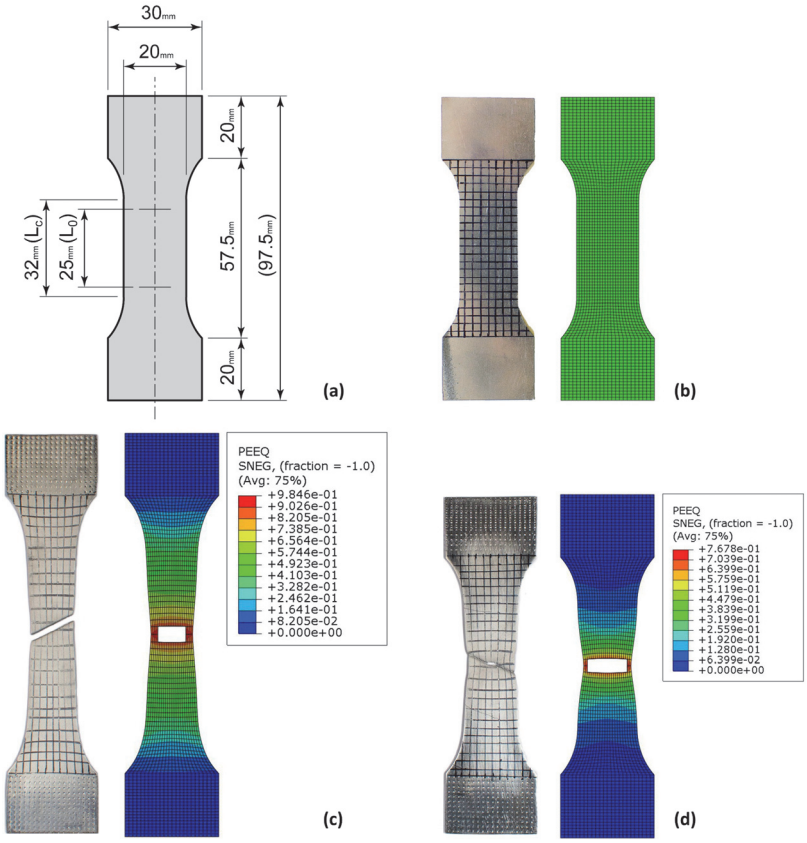

Figure 5: Rectangular cross-section tensile specimens used to perform both the tensile tests and their FEM simulations. Dimensioned drawing of the specimen (a), real specimen and finite element simulation before tensile tests (b), real specimen and finite element simulation in AISI 304 (c) and in AISI 430 (d) after tensile tests.

Constitutive models

The constitutive models of AISI 304 and AISI 430 steels were implemented according to ABAQUS® theory manuals [23]. The quasi-static nature of both the tensile tests and the Erichsen tests is evident, therefore allowing to create rate-independent constitutive models. Moreover, the ductile behaviour of the considered materials in quasi-static regime allows to model their tensile behaviour as elastic-plastic with non-linear hardening. Considering that both tests have their focus on the measurement of the static response of the samples until failure, it is evident that a damage and failure model must be introduced to be able to predict the ultimate condition of both tensile and Erichsen tests. The two materials have qualitatively

similar tensile behaviour; therefore, both were associated with the same kind of model, parameterized as follows, and a simulation of the tensile test was used to validate their accuracy in predicting the elastic-plastic response until failure. The validated models were then associated with the Erichsen tests specimens to conduct the deep drawing simulations.
The elastic modulus was estimated from the slope of the experimental stress/strain curves resulting from the tensile tests. The Young's moduli were estimated as 195 GPa and 220 GPa for AISI 304 and AISI 430 respectively.
Both were associated with 0.3 Poisson's ratio. The elastic parameters were implemented in the simulations by means of the *ELASTIC keyword according to ABAQUS®/Standard [23] theory.
The plastic and hardening behaviour was parameterized in terms of tabulated true stress and plastic true strain values by means of the *PLASTIC keyword according to ABAQUS®/Standard [23] theory, with three stress/strain pairs representing the yield point, the ultimate stress, and an intermediate point between them to catch the slight non linearity of the hardening process. The values of the true plastic strain corresponding to the ultimate stress is also the parameter that triggers the softening of the materials leading to necking and failure, therefore its value is the fundamental parameter given in the simulations by means of the *DAMAGE INITIATION keyword, which is used to provide material properties that define the initiation of damage. In the case considered a CRITERION=DUCTILE was used without the LODE DEPENDENT parameters. The following phases are governed by the evolution of the damage manifesting itself as the softening of the material. This progressive deterioration of the tensile strength is modelled as a damage function f, having null value before the maximum stress σ_R^* and increasing its value during the softening phases until it reaches a unit value once the material has no residual strength left and the break happens (eq. 3). For both AISI 304 and AISI 430, this damage function f was parameterized by means of the *DAMAGE EVOLUTION keyword considering the independent variable of the damage function being the plastic displacement after the initial failure (TYPE=DISPLACEMENT option), and its non-linear evolution was implemented by means of tabulated points (damage, plastic displacement according to the SOFTENING=TABULAR option) where the damage is the decrease ratio of the stress curve during the softening phase compared to the ultimate true stress, and the plastic displacement variable is the increase of the true plastic strain from the damage initiation point, multiplied to the initial axial length of the parallel length of the specimen (L_c = 32 mm):

$$\text{f = damage function} = \frac{\sigma_R^* - \sigma^*}{\sigma_R^*} \tag{3}$$

$$\text{d = plastic displacement} = \left(\varepsilon_{pl}^* - \varepsilon_{plR}^*\right) \cdot L_c \tag{4}$$

This way the local damage evolution is tracked during the simulation independently from the size of the elements, and the softening of the failed elements is consistent. In Tab. 3 a summary of the material parameters, and in Fig. 6 the comparison between experimental stress/strain curves and the models.

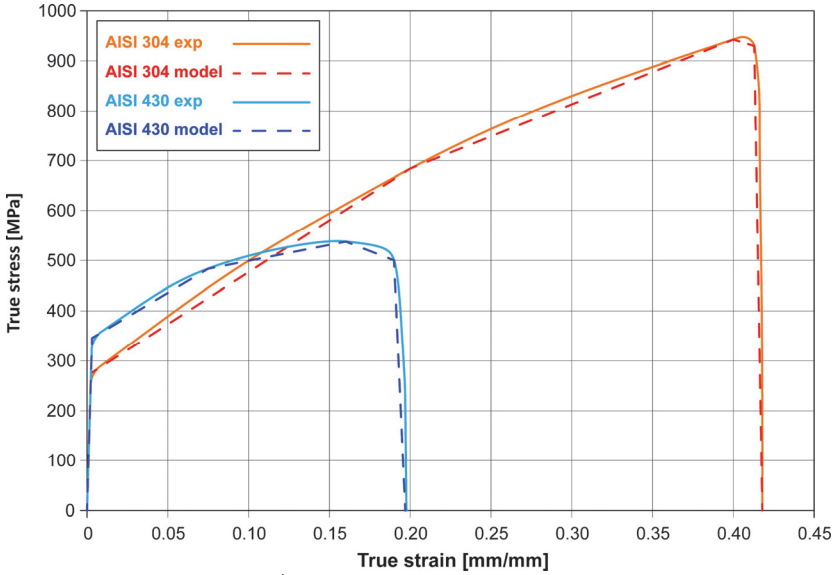

Figure 6: Comparison between the true stress /true strain curves of the constitutive models and the experimental curves.

It is important to notice that the value of L_c is the main calibration parameter regulating the elongation due to necking. So, in general, it is possible to conduct trial and error tests by varying that parameter to calibrate the elongation before break. In our case L_c = 32 mm was consistent with no need to further calibration for both materials, in fact the results of the tensile test simulations in terms of Load/Displacement curves allowed to validate those material models and parameters (Fig. 7).

Condition	AISI 304				AISI 430			
	σ* [MPa]	ε*$_{pl}$ [mm/mm]	Damage *f*	Displacement *d* [mm]	σ* [MPa]	ε*$_{pl}$ [mm/mm]	Damage *f*	Displacement *d* [mm]
YIELD	270	0	-	-	340	0	-	-
HARDENING	680	0.200	-	-	485	0.075	-	-
FAILURE	945	0.400	0	0	540	0.160	0	0
SOFTENING	930	0.415	0.015	0.320	500	0.190	0.070	0.960
BREAK	0	0.420	1.000	0.575	0	0.195	1.000	1.185

Table 3: Parameters associated with the constitutive models representing the plastic and damage behaviors of AISI 304 and AISI 430 as implemented in the simulations.

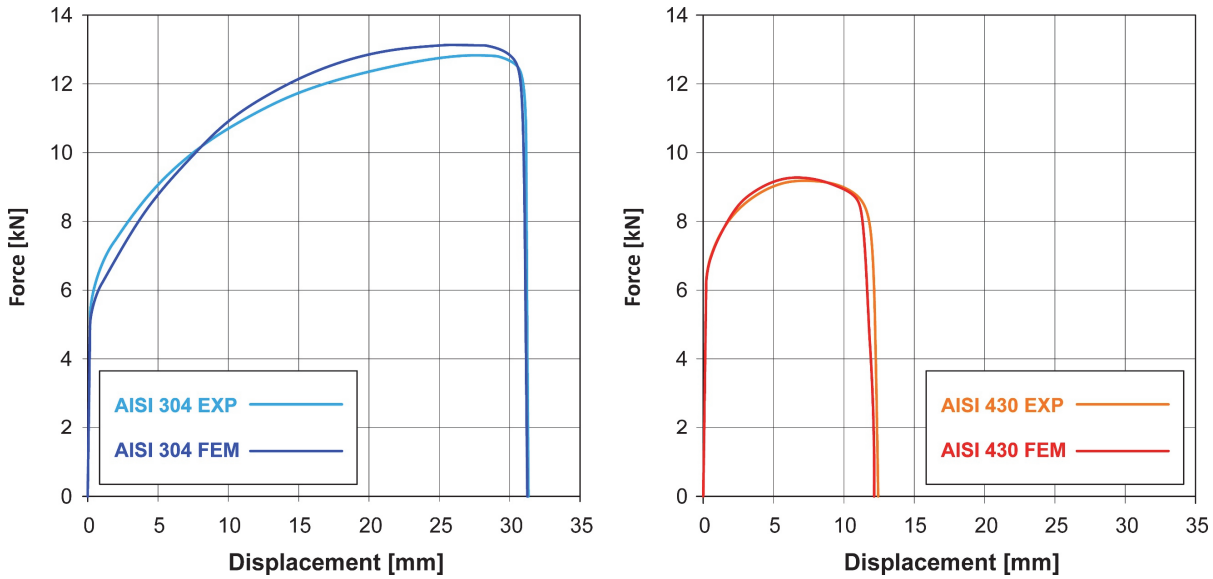

Figure 7: Comparison between the experimental and numerical tensile test load-displacement curves used to validate the material models; AISI 430 (left) AISI 304 (right).

ERICHSEN TESTS

The Erichsen tests were performed with a dual purpose: on one hand, they evaluate the effect of the material and lubrication on the deep drawing of AISI 304 and AISI 430 sheets, while on the other hand they calibrate the FEM model dedicated to deep drawing by comparing the experimental and numerical results. The tests were performed according to the EN ISO 20482 standard, using the experimental setup illustrated in Fig. 8. To evaluate the effect of lubrication, two conditions were compared:

- without lubrication between the sheet metal, punch and blank holder (condition identified by the letter **D**);
- lubrication with PVC film placed on the sheet metal both in the punch area and in the blank holder area (condition identified by the letter **P**).

The punch feed rate and the blank holder pressure were set to the lower limit expected by the testing machine, equal to 4.3 MPa and 6.57 MPa respectively. These settings increase the IE values, enhancing the differences between the materials and the lubrication types under examination [6]. For each experimental condition, three replicates were performed, for a total of 12 completely randomized tests according to the Design of Experiment [24]. The results were first summarized

graphically in Fig. 9 (individual value plot, main effects plot and interaction plot) and then statistically analyzed by ANOVA (Analysis of Variances) [24] up to second-order interaction, whose results are reported in Tab. 4 (p-value equal to 0.05). The hypotheses of normality, homoscedasticity and independence were also verified without highlighting problems.

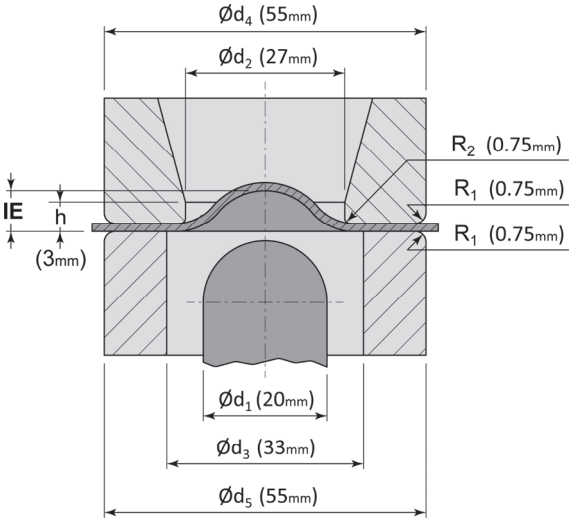

Figure 8: Section of a generical Erichsen testing machine. d_1 is the diameter of the punch, while d_2 and d_3 represent the internal diameter of the die and the blank holder. R_2 is the internal radius of the blank-holder. The result of the test is represented by the depth of the spherical cup (IE).

Both the preliminary graphical analysis (Fig. 9) and the ANOVA (Tab. 4) show that AISI 304 has higher Erichsen indices (IE) than AISI 430. The former, in fact, highlights significantly higher "n" and "A_g%" values, which distribute local stresses due, for example, to imperfections in the sheet metal, non-uniform lubrication, or geometric errors in the die, preventing both localized necking and unwanted breakages during deep drawing. The PVC solid lubricant also significantly increases the Erichsen index, thanks to the improved sliding of the sheet metal in contact with the punch and the greater amount of steel that flows from the blank holder.

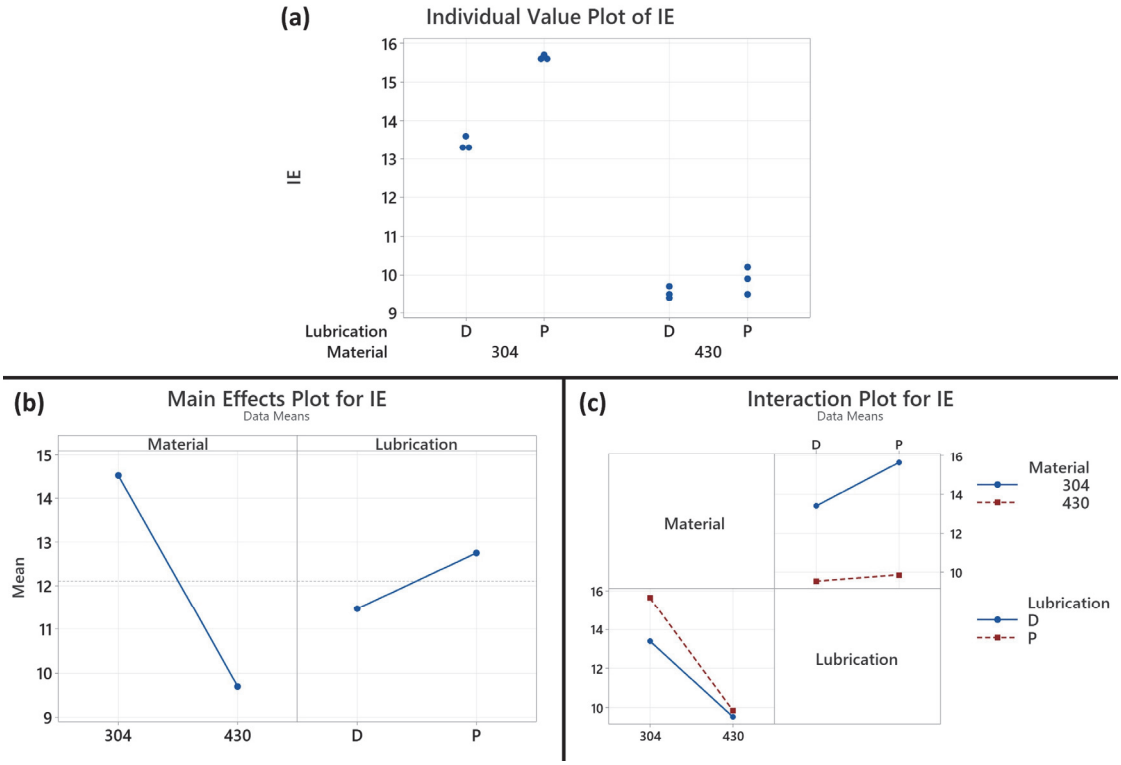

Figure 9: Effect of material and lubrication on the Erichsen index (IE). (a) Preliminary visual analysis of the data - Individual Value Plot, (b) main factors - Main Effect Plot and (c) interactions - Interaction Plot.

Source	DF	Adj SS	Adj MS	F-Value	P-Value
Material	1	69,6008	69,6008	1546,69	0,000
Lubrication	1	4,9408	4,9408	109,80	0,000
Material*Lubrication	1	2,7075	2,7075	60,17	0,000
Error	8	0,3600	0,0450		
Total	11	77,6092			

Table 4: ANOVA table of the main factors (material and lubrication) and their interactions up to the second order. In green the significant factors and interactions according to a p-value lower than 0.05.

The Erichsen index provides a practical and easy-to-use result, but it does not provide information on the deformation patterns of the sheet metal during the deep drawing process. To obtain this information, a rectangular array of 2.5 mm diameter circles was screen-printed onto the sheet metal surface, and their geometric change was measured after the Erichsen test. Specifically, the circumferences lying on a line passing through both the fracture zone and the apex of the spherical cap produced by the test were evaluated (Fig. 10), and the change was detected along the diameters parallel and perpendicular to the reference line.

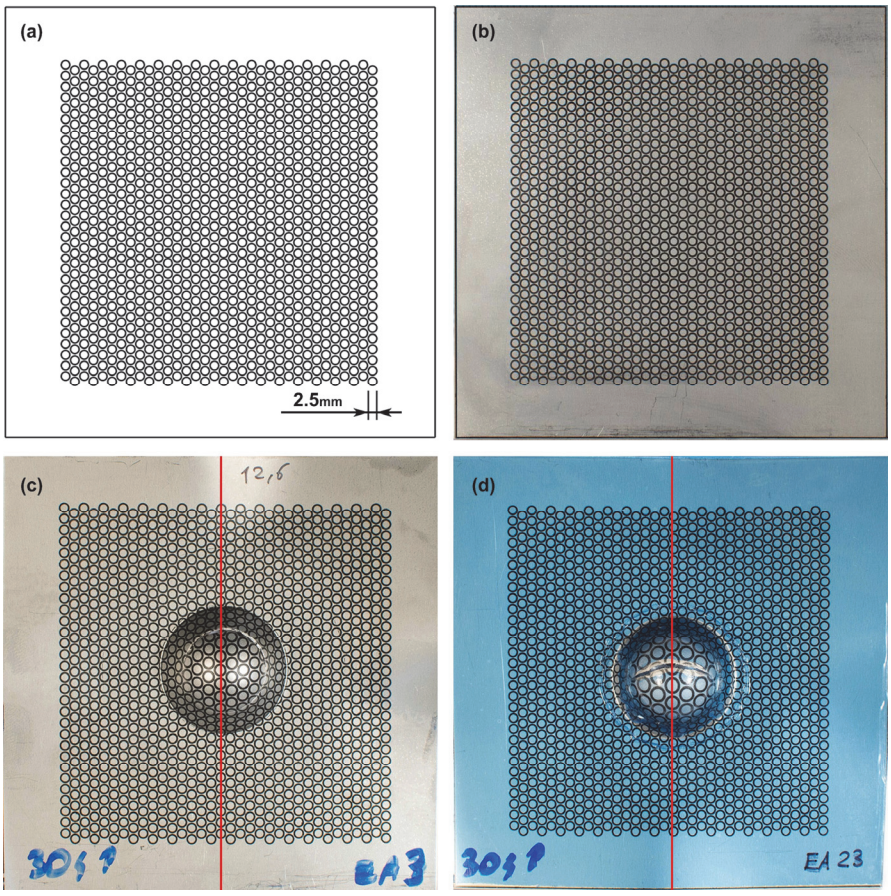

Figure 10: Technical drawing of the screen-printed sample used for the Erichsen tests (a), image of the sample before (b) and after the Erichsen test (c-d). Images c and d show AISI 304 samples in unlubricated and PVC-lubricated conditions, respectively. The circumferences intercepted by the red lines were used to measure the diameters in the longitudinal and transverse directions to the line.

The measurements were performed using a LEICA® M165C stereomicroscope with 10x magnification and graduated paper with a resolution of 200 µm applied to the profile of the cap. The same samples were also used to measure the thickness of the spherical cap at the circumferences used to evaluate in-plane deformations.

To this end, the samples were first cold-sectioned and then mirror polished using abrasive papers (120, 320, 400, 600, 800, and 1200 grit) and polishing cloths with synthetic diamond abrasive (3 μm and 1 μm grit). Lubrication was ensured using water for the papers and abrasive suspension for the cloths. The etching was carried out chemically using Vilella reagent (hydrochloric acid, 5 mL, picric acid, 1g, and ethanol, 100mL), for AISI 430, and electrochemically with a solution of 10 g of oxalic acid in 100 mL of distilled water, for AISI 304. Both images and thickness measurements were acquired using a LEICA® DM4000M optical microscope at 5x magnification.

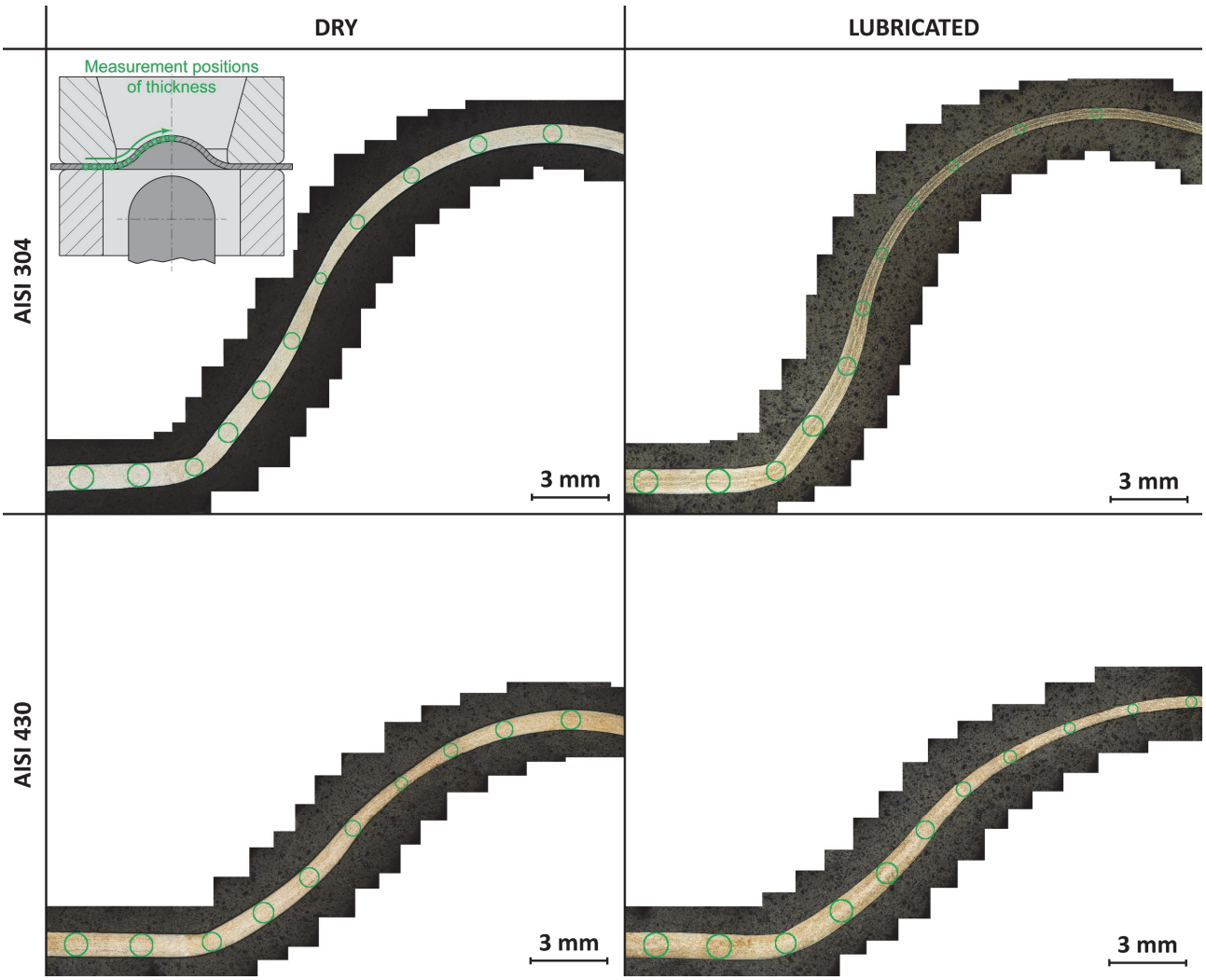

Figure 11: Metallographic analyses at low magnification (5x) of the spherical cap profile after the Erichsen tests: the green circles show the areas where the dimensional analyses were performed. For AISI 430 the etching was carried out by immersion in a solution of 5 ml of hydrochloric acid and 1 g of picric acid in 100 mL of ethanol. For AISI 304 the etching was carried out electrochemically with a solution of 10 g of oxalic acid in 100 mL of distilled water.

The profiles of the spherical caps and the in-plane and thickness strain are summarized in Fig. 11, Fig. 12 and Fig. 13. The images confirm that both material and lubrication have a significant effect on the sheet metal deformation. In unlubricated specimens, friction in the contact areas with the blank holder and the punch is so high that it allows very little deformation which is concentrated between these two zones where the steel can deform freely. This behaviour is well described for both stainless steels by both the profile of the Erichsen specimens (Fig. 11) and the in-plane deformation (Fig. 12), which follows a different trend for each area of the specimen. While longitudinal and transverse deformations are practically zero below the blank holder, they reach values of approximately 10% in both directions at the end of the punch, indicating limited deformation due to balanced biaxial stretching. Between the blank holder and the punch, deformation occurs by drawing, with longitudinal strains reaching positive values between 40% and 80%, while transverse strains are negative by approximately 10%. In unlubricated specimens, the longitudinal strain profile takes on a "double bell" shape, as maximum deformation and failure occur on a circumference approximately halfway between the blank holder and the punch. The use

of a solid lubricant with a PVC film dramatically changes the strain profile, which, in both directions, is similar and increases almost steadily up to the tip of the punch. In this case, deformation occurs everywhere due to balanced biaxial stretching. In specimens lubricated with PVC film, both longitudinal and transverse strains take on a "single bell" shape, with maximum deformation and failure occurring near the apex of the spherical cap. The type of stainless steel also plays a significant role: AISI 304, thanks to its greater plastic deformability and high work hardening coefficient distributes deformations better than AISI 430. Similar considerations can also be extended to the thickness of the sheet metal, summarised in Fig. 13 on the side of the spherical cap not affected by the fracture.

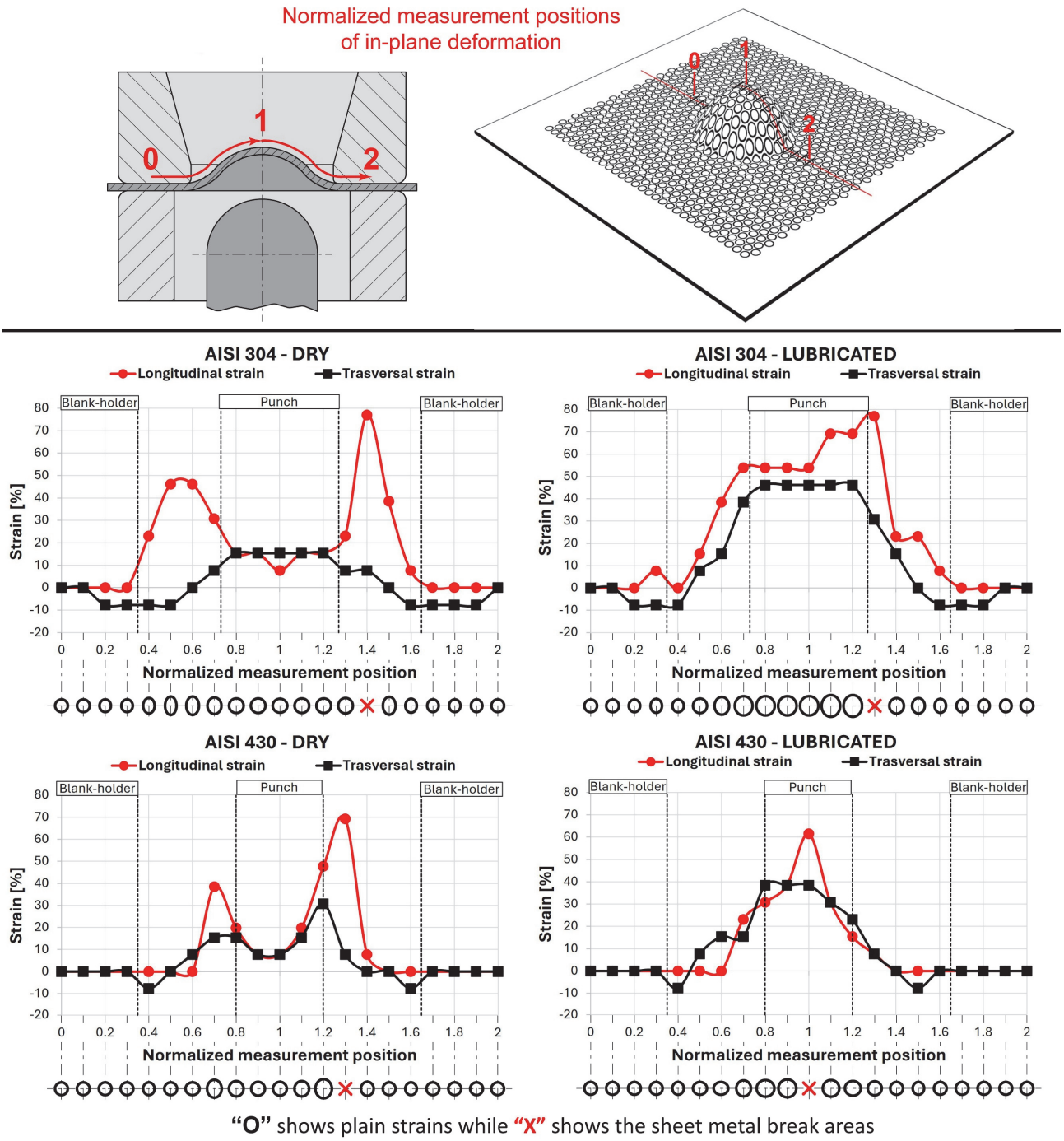

Figure 12: Planar deformations of the spherical cap generated by the Erichsen test. To allow comparison between different experimental conditions, the measurement positions were normalized with respect to the total length of the deformed zone. Position 1 indicates the apex of the cap, while positions 0 and 2 correspond to the blank holder. The circles shown below the graphs indicate the deformation of the sheet metal at each measurement point.

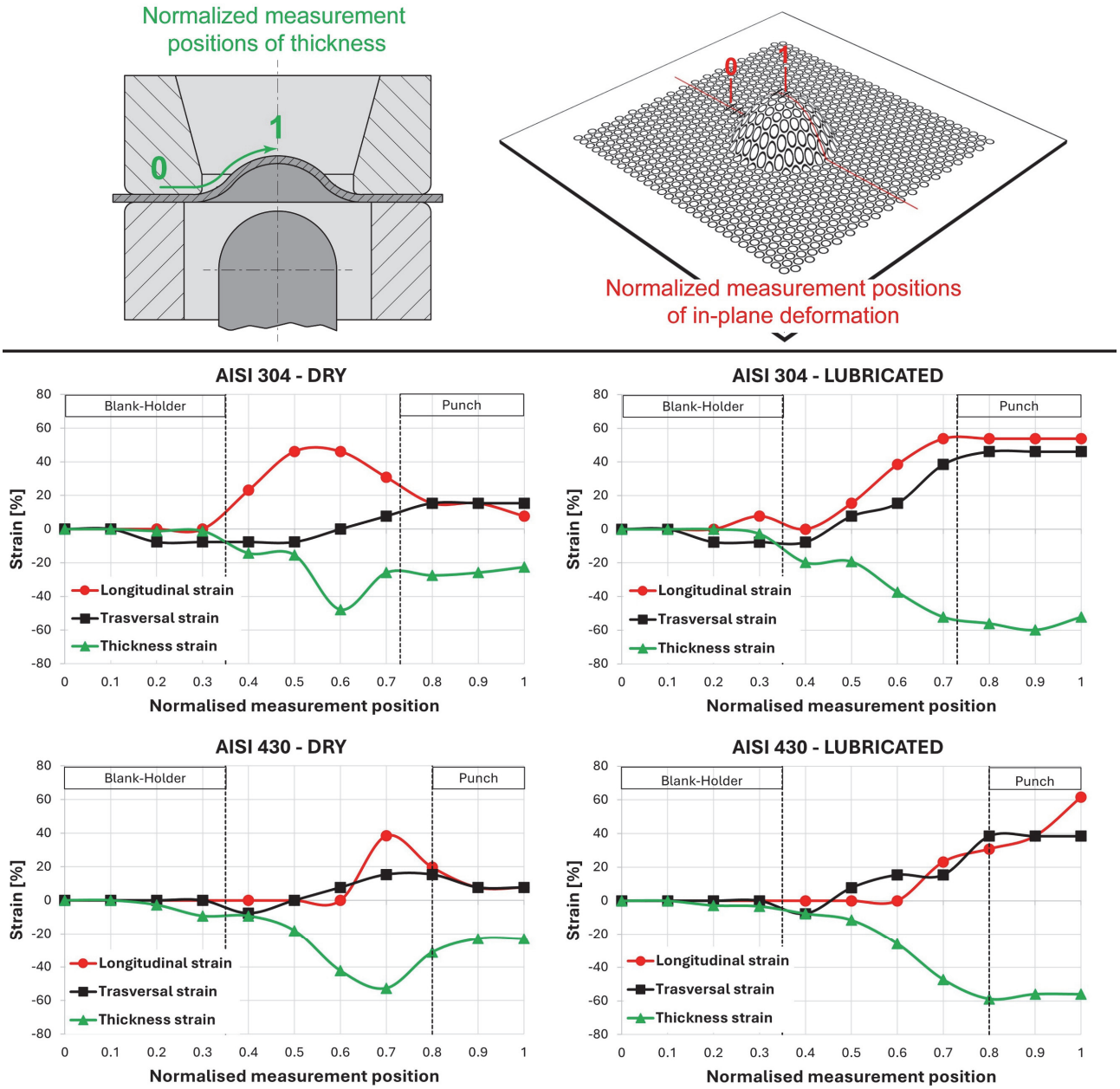

Figure 13: Planar deformations and thickness of the spherical cap generated by the Erichsen test. To allow comparison between the different experimental conditions, the position of the measurements was normalized with respect to the length of the deformed zone between one of the two blank holders and the apex of the spherical cap. Position 1 indicates the apex of the cap, while position 0 indicates the blank holder. The image only considers the half of the cap not affected by the crack.

FEM Analysis of the Erichsen Tests

The results shown in the previous paragraphs were used to calibrate the finite element model of an Erichsen test by varying steel and lubrication. This step is very important for the development of a model dedicated to the simulation of deep drawing processes. The geometry of the sheet metal, the punch, and the blank holder were modelled as shells using the ABAQUS®/CAE software (Fig. 14-a) respecting the dimensions of the real testing machine defined in Fig. 8. The sheet metal was discretized using three-node 3D shell finite elements (S3R type) of size between 3.6mm (periphery of the specimen) and 0.4mm in the areas beneath the blank holder and the punch (Fig. 14-b). Exploiting the geometric

symmetry of the system, a quarter of the assembly was modeled, applying symmetry boundary conditions to the nodes located on the symmetry planes (Fig. 14-c).

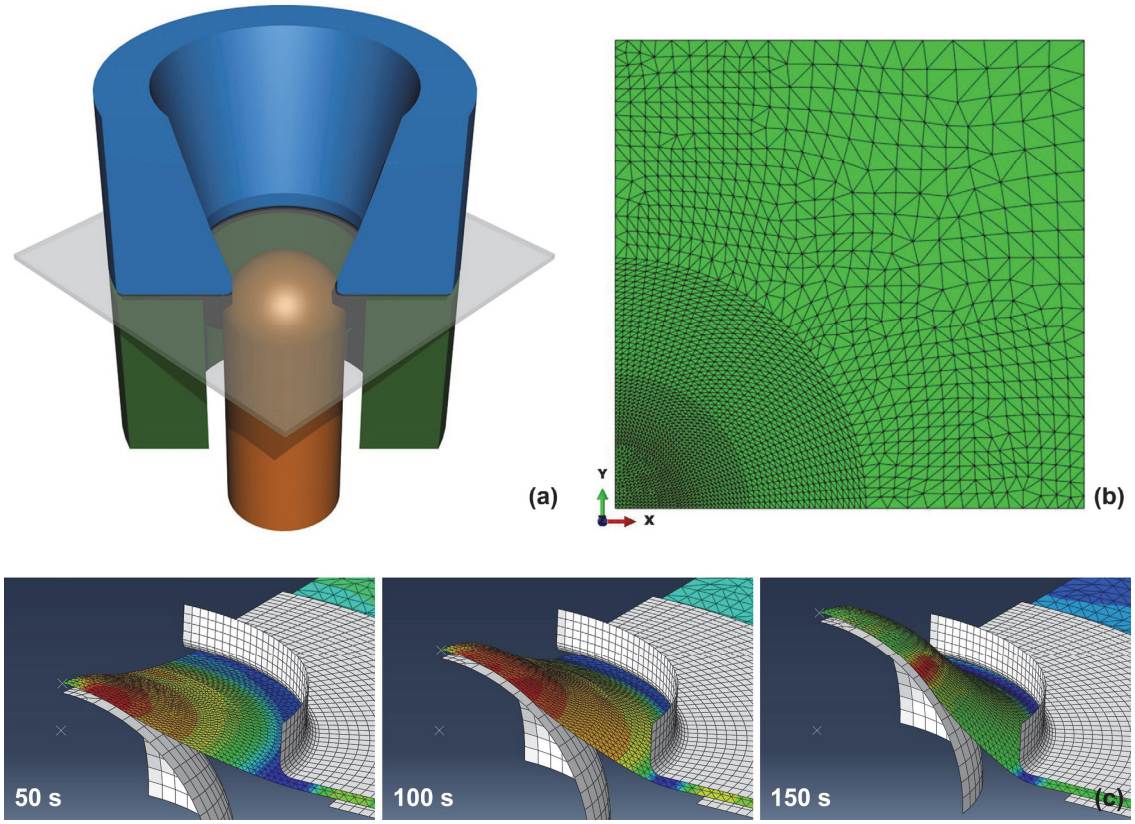

Figure 14: (a) CAD model of the main components of the system used to perform the Erichsen tests. (b) Mesh used to discretize the sheet metal. (c) Example of punch movement during the Erichsen test simulation at three different times (50 s, 100 s and 150 s). A quarter of the model was analyzed by applying symmetry boundary conditions on the symmetry planes.

The mechanical behaviour of the sheet metal was assured by the constitutive models above discussed and validated for the tensile tests. The Erichsen test stops when the sheet metal cracks, which occurs for true stresses and strains exceeding the physical breaking point of the material. The punch and blank holder were modelled as infinitely rigid bodies since their deformation is negligible compared to that of the sheet metal and are not the subject of research.

The contact interactions between sheet metal, punch and blank holder were modelled by adopting a thickness-sensitive surface-to-surface penalty algorithm, with the sheet metal having slave role to maximize the accuracy and the convergence. For sliding conditions without lubrication or with lubrication by PVC film, friction coefficients of 0.75 and 0.20 respectively were used, representative of the contact between steel surfaces with 2B finish [25] and between PVC and steel.

The simulation was performed using the non-linear implicit solver of ABAQUS®/Standard [23], the simulation involves two main phases, the first one being the pre-load of the blank holder to stabilize the specimen, and the second phase being the progressive rigid displacement of the punch to establish contact with the specimen and lead its deformation. The pre-load phase was simulated as an implicit step during which the blank holder is gradually loaded until the entire preload force is applied. An automatic incremental strategy is activated so that the solver can control the extent of the increments based on the convergence and in particular to reduce the increment to easily reach the convergence of the contact at the beginning of the step and then increase it once the static equilibrium is established to finalize the full pre-load efficiently. The second phase is an implicit step based on the prescribed motion of the punch, again with an automated incremental strategy to minimize the computational time to reach the convergence of the initial contact and to maintain the calculation stable during the progressive deformation and relative sliding of the punch and sheet metal. The motion of the punch is applied at constant speed over a period of 200 non-physical time units to allow an easy comparison with the real phases of the Erichsen test, spanning around 200 seconds.

The finite element analyses produced results very close to those measured experimentally for the IE index, with an average error of less than 3% (Tab. 5). The location of the fracture (Fig. 15) as well as the deformation trend along the plane and

thickness are similar to those detected in reality (Fig. 16). The FEM model faithfully reproduces both the "double bell" profile, typical of deformation without lubrication where the fracture occurs on a circumference approximately halfway between the punch and the blank holder, and the "single bell" profile obtained using the lubrication with a PVC film, thanks to which the fracture moves near the apex of the spherical cap.

Material	Lubrification	IE experimental	IE FEM	Error [%]
AISI 304	D	13.4	14.2	+ 6.0
AISI 304	P	15.6	15.2	- 2.5
AISI 430	D	9.5	9.2	- 3.2
AISI 430	P	9.9	9.9	0.0

Table 5: Comparison between the results of the real Erichsen test and the one simulated by FEM.

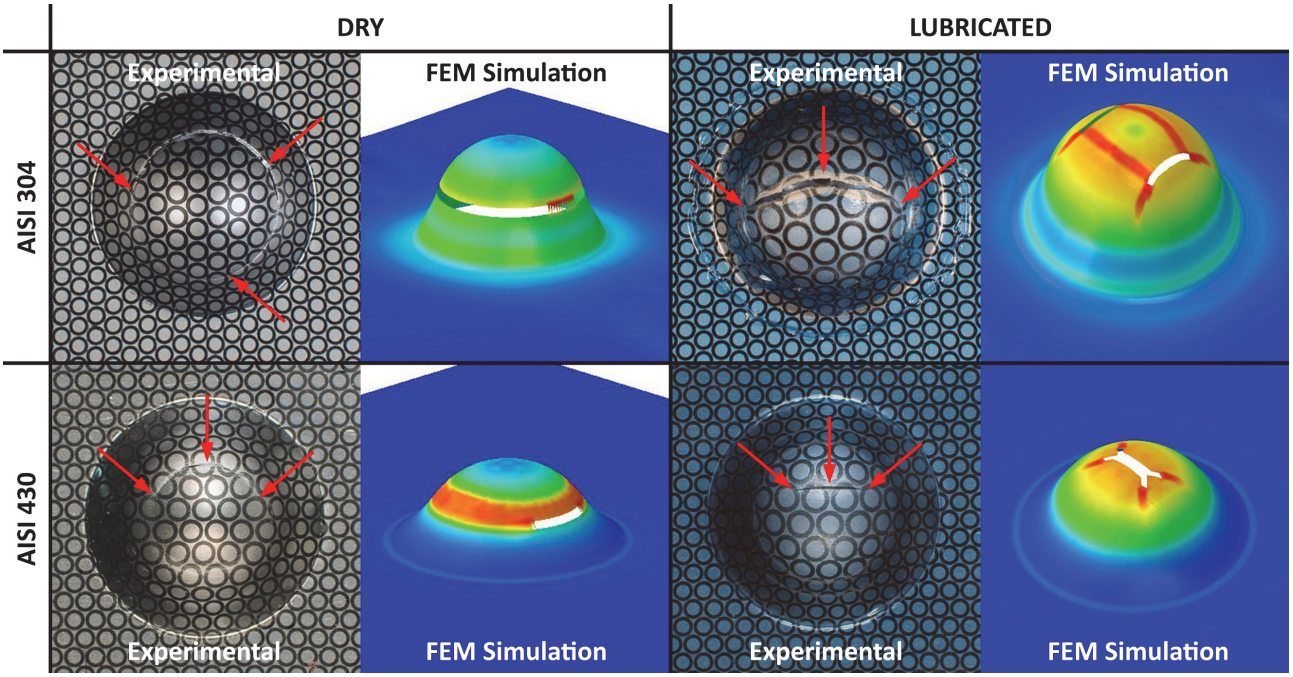

Figure 15: Comparison between the deformations after the experimental Erichsen test (left) and the simulated one (right) for each experimental condition. The crack location in the actual samples is highlighted by red arrows.

After verifying its correct functioning, the FEM model was used to estimate the stresses immediately before failure (Fig. 17) and to simulate the evolution of the sheet thickness over time in technically significant areas (Fig. 18). Regarding stresses, the FEM simulation shows a similar trend to that observed for deformations. Without lubrication, the Von Mises stresses follow a "double bell" profile, with a peak above 1000 MPa located in the area between the blank holder and the punch. Using a solid lubricant with a PVC film, the simulation returns a "single bell" trend, with a nearly constant increase from the blank holder to the apex of the spherical cap, where the Von Mises stresses exceed 1200 MPa. The type of stainless steel is also an important factor, which cannot be overlooked in the stress analysis. Thanks to its higher plastic deformability and high work hardening coefficient, AISI 304 is able to distribute stresses more uniformly than AISI 430, which instead tends to concentrate them in a more localized way.

The evolution of sheet metal thickness over time has been studied in the four areas listed below.

- **Area A:** below the blank holder;
- **Area B:** near the knee, just beyond the blank holder;
- **Area C:** free from contact with both punch and blank holder;
- **Area D:** apex of the spherical cap.

The test time was normalized between the values 0 and 1, corresponding respectively to the contact of the punch with the sheet metal and the end of the Erichsen test, determined by the sheet metal cracking.

The simulation results, shown in Fig. 18, highlight that the first area to deform is always the one underneath the punch (zone D), regardless of the steel type and lubrication methods. At the beginning of the test, it is necessary to create a cap that reproduces the spherical shape of the punch.

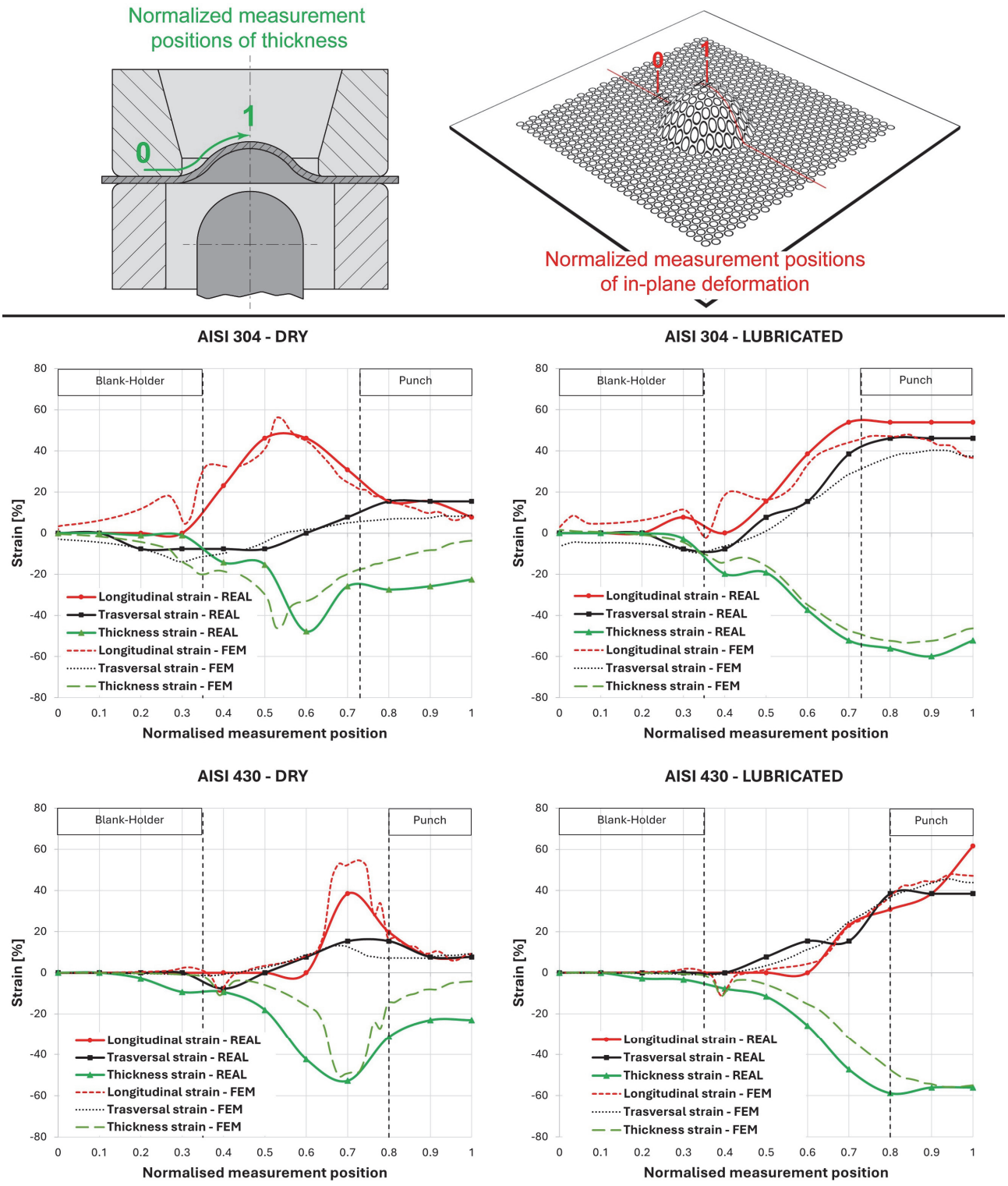

Figure 16: Comparison between the experimentally measured deformations (solid lines) and those predicted by the FEM simulation (dashed lines). To allow comparison between the different experimental conditions, the position of the measurements has been normalized with respect to the length of the deformed zone between one of the two blank holders and the apex of the spherical cap. Position 1 indicates the apex of the cap, while position 0 indicates the blank holder. The image only considers the half of the cap not affected by the crack.

Of greater interest is what happens subsequently, when a clear difference between the two lubrication methods is noted: without lubricant, the thickness in zone D does not decrease further, while a significant thinning occurs between the punch and the blank holder (zone C) that continues until failure. For the specimens lubricated with PVC film, the reduction in thickness underneath the punch (zone D) continues until the sheet metal cracks. Lubrication also allows for better strain distribution, resulting in a significant reduction in thickness in areas B and C, as well as D. The FEM simulation also highlighted that, unlike AISI 430, AISI 304 shows a significant thinning near the knee (area B) and a slight reduction in thickness in the area beneath the blank holder (area A). These differences are due to the higher plastic deformability and high work hardening coefficient of AISI 304, which allow it to distribute both stresses and strains more effectively and homogeneously than AISI 430.

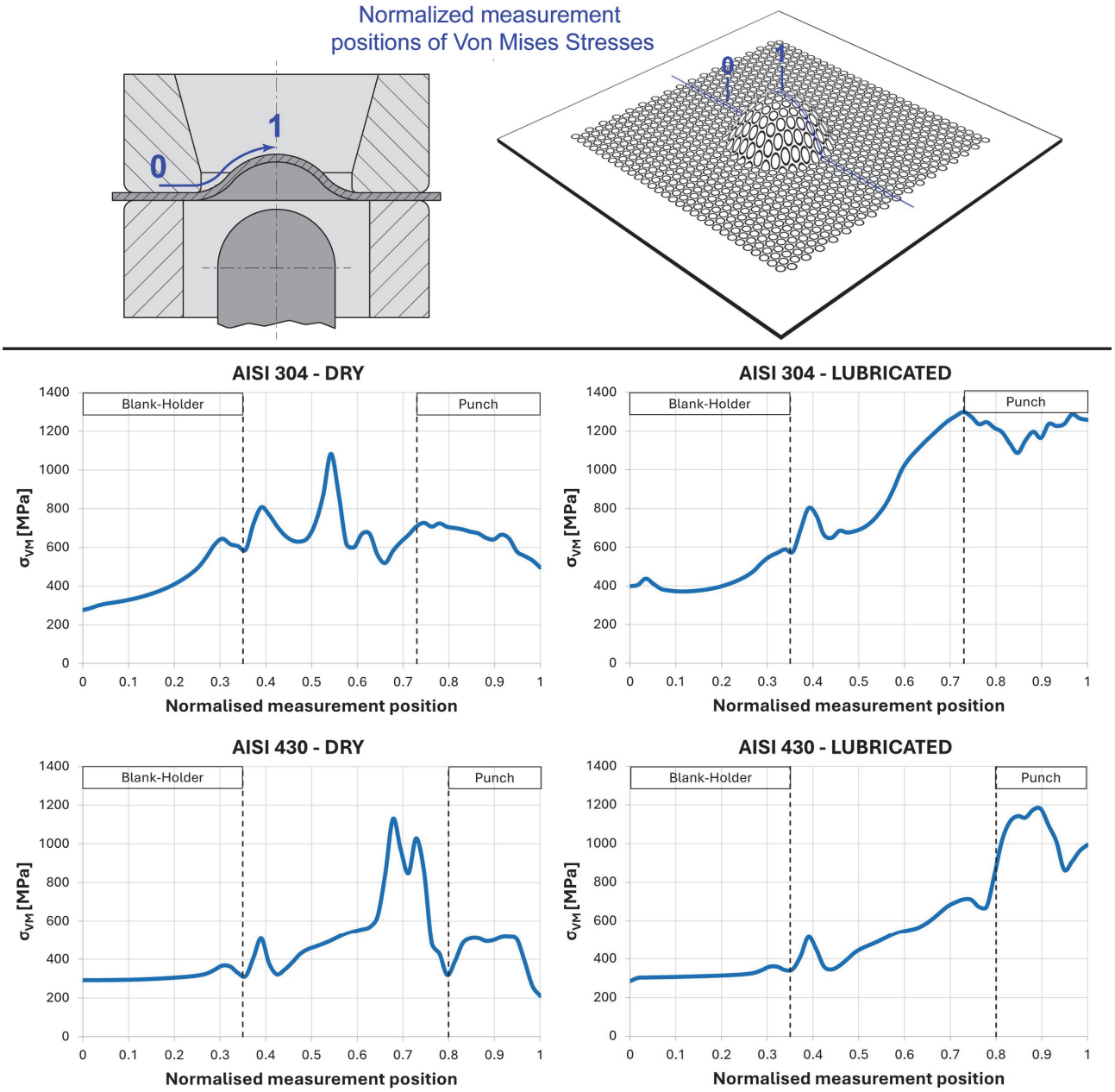

Figure 17: Von Mises stresses predicted by the FEM analysis immediately before the spherical cap failed. To allow comparison between the different experimental conditions, the measurement position was normalized with respect to the length of the deformed zone between one of the two blank holders and the apex of the spherical cap. Position 1 indicates the apex of the cap, while position 0 indicates the blank holder. The image only considers the half of the cap not affected by failure.

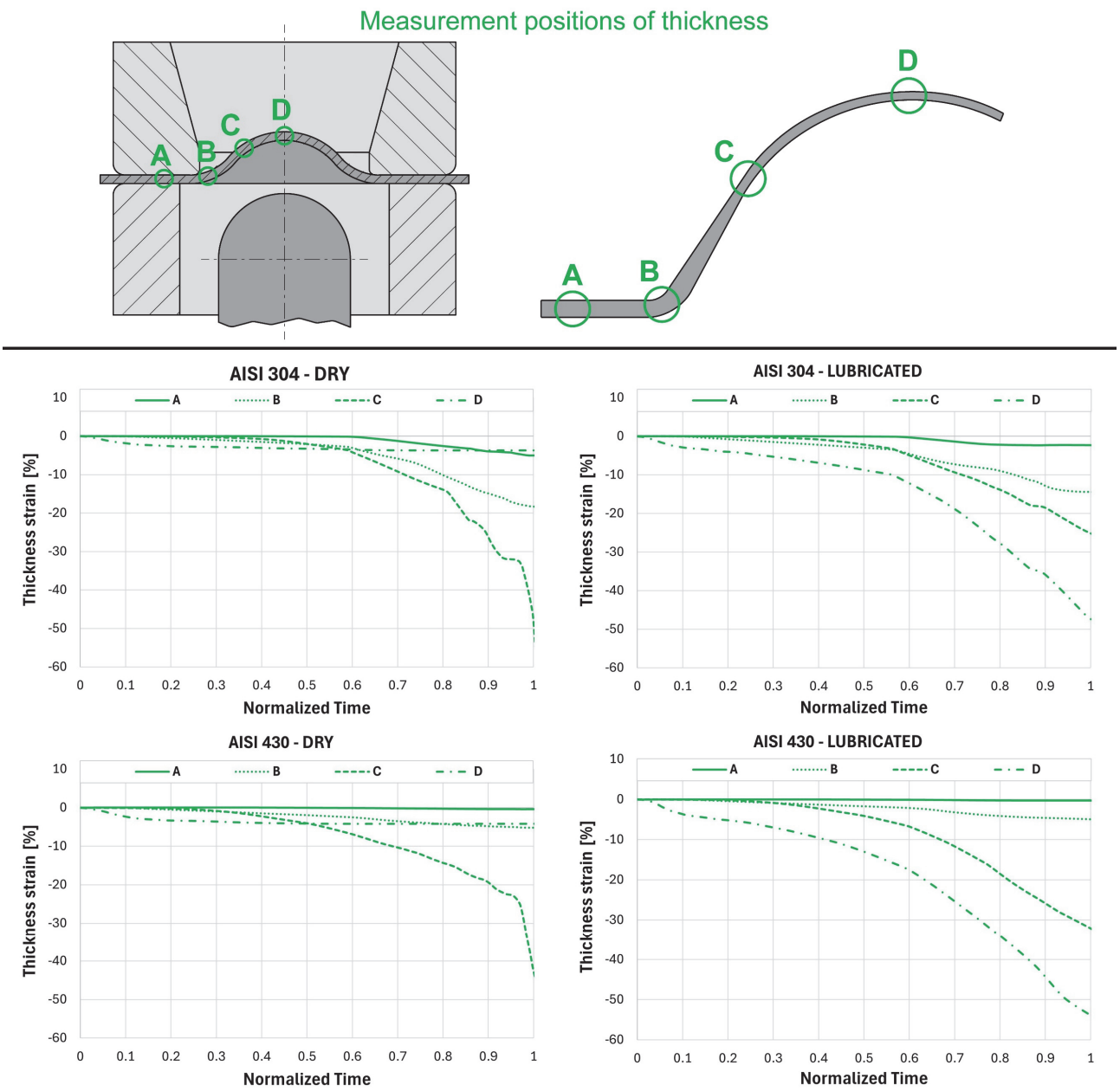

Figure 18: Thickness reduction over time predicted by the FEM analysis. To allow comparison between the different experimental conditions, the test time was normalized between the values 0 and 1, corresponding respectively to the contact of the punch with the sheet metal and the end of the Erichsen test, determined by the cracking of the sheet metal.

Conclusions

This research led to the development of a FEM model for simulating deep drawing under different operating conditions, stainless steel, and lubrication. The model was calibrated by simulating a series of Erichsen tests on AISI 304 and AISI 430 stainless steel sheets under different lubrication conditions, and then comparing the experimentally in-plane deformations and thicknesses with those predicted numerically. To ensure the accuracy of the true stress-strain curves, both stainless steels were characterized through tensile tests, Erichsen tests, and metallographic analyses of the cold-formed samples. To this end, a method was developed that provides an accurate representation of the stainless steel's true stress-strain curve beyond necking. The experiment was structured according to the principles of Design of Experiments (DoE) for full and orthogonal planes, replicated three times, while the statistical analysis was conducted using the ANOVA (Analysis of Variance) technique.

The conclusions resulting from the research are reported below.

- The finite element model produced extremely accurate results, with an average error of less than 3% compared to experimental data for the IE index. Other parameters, such as fracture location, in-plane strains, stresses, and spherical cap thickness, are also very similar to those observed experimentally. For both AISI 304 and AISI 430, the model faithfully replicated two distinct scenarios:
  - *"Double bell"* profile: typical of stresses and deformations obtained without lubrication, where the breakage occurs on a circumference halfway between the punch and the blank holder.
  - "Single bell" profile: obtained by using a solid lubricant with a PVC film, which moves the fracture close to the apex of the spherical cap.
- The experimental technique developed to determine the true stress-strain curve of steel from necking to physical fracture of the specimen has proven to be extremely effective and technically simple. The geometry and mesh of the virtual tensile specimens faithfully reproduce the shape of the real specimens and the distribution of the grid printed on the parallel length before the test. The accuracy of the true stress-strain curve for both AISI 304 and AISI 430 is also confirmed by the excellent performance demonstrated by the FEM model used to simulate the deep drawing process.
- Lubrication has a significant impact on sheet metal deformation. In unlubricated specimens, the high friction in the contact zones between the blank holder and the punch severely limits deformation, which instead is concentrated in the intermediate zone where the material can deform freely. Below the blank holder, longitudinal and transverse deformations are practically zero, while at the tip of the punch they reach approximately 10% in both directions, showing limited balanced biaxial elongation. Between the blank holder and the punch, deformation occurs by deep drawing, with longitudinal deformations reaching 40-80% and transverse deformations around -10%. In contrast, the use of a solid lubricant with a PVC film radically changes the process: deformation continues to increase up to the tip of the punch in both directions. In this case, the sheet metal deforms everywhere by balanced biaxial elongation.
- The type of stainless steel also plays an important role: AISI 304, thanks to its greater plastic deformability and high work hardening coefficient, distributes deformations better and more homogeneously (both in the plane and along the thickness) than AISI 430.
- The stresses highlight a similar pattern to the strains. Without lubrication, the Von Mises stresses show a *"double bell"* profile, with peaks exceeding 1000 MPa between the blank holder and the punch. In contrast, using a solid lubricant with a PVC film, the simulation shows a *"single bell"* pattern that increases almost continuously from the blank holder to the apex of the spherical cap, where the stresses exceed 1200 MPa. The type of stainless steel also plays a crucial role: AISI 304, thanks to its greater plastic deformability and high work hardening coefficient, distributes stresses more uniformly than AISI 430, which tends to concentrate them in specific points.

REFERENCES

[1] Ikumapayi, O.M., Afolalu, S.A., Kayode, J.F., Kazeem, R.A., Akande, S. (2022). A concise overview of deep drawing in the metal forming operation., Materials Today: Proceedings, 62, pp. 3233–3238.

[2] Tiwari, P.R., Rathore, A., Bodkhe, M.G. (2022). Factors affecting the deep drawing process – A review, Mater Today Proc, 56, pp. 2902–2908. DOI: https://doi.org/10.1016/j.matpr.2021.10.189.

[3] Kim, H., Sung, J.H., Sivakumar, R., Altan, T. (2007). Evaluation of stamping lubricants using the deep drawing test, Int J Mach Tools Manuf, 47(14), pp. 2120–2132. DOI: https://doi.org/10.1016/j.ijmachtools.2007.04.014.

[4] Kim, H., Altan, T., Yan, Q. (2009). Evaluation of stamping lubricants in forming advanced high strength steels (AHSS) using deep drawing and ironing tests, J Mater Process Technol, 209(8), pp. 4122–4133. DOI: https://doi.org/10.1016/j.jmatprotec.2008.10.007.

[5] Wifi, A.S., Abdelmaguid, T.F., El-Ghandour, A.I. (n.d.). A review of the optimization techniques applied to the deep drawing process.

[6] Casaroli, A., Scabini, E., Boniardi, M., Gerosa, Ri., Rivolta, B. (2025). Optimization of austenitic and ferritic steels for deep drawing: Part 1: metallurgical and mechanical analyses., Fracture and Structural Integrity, 20(75), pp. 104–125. DOI: https://doi.org/10.3221/IGF-ESIS.75.09.

[7] Andreotti, R., Quercia, M., Casaroli, A., Boniardi, M. V. (2023). Load history estimation for ballistic impacts with bullet-splash., Procedia Structural Integrity, 51, pp. 37–43.

[8] Andreotti, R., Casaroli, A., Quercia, M., Boniardi, M. V. (2022). A simplified formula to estimate the load history due to ballistic impacts with bullet splash. Development and validation for finite element simulation of 9x21mm full metal jacket bullets, Frattura ed Integrita Strutturale, 16(62), pp. 602–612. DOI: https://doi.org/10.3221/IGF-ESIS.62.41.
[9] Andreotti, R., Casaroli, A., Colamartino, I., Quercia, M., Boniardi, M.V., Berto, F. (2023). Ballistic Impacts with Bullet Splash—Load History Estimation for.308 Bullets vs. Hard Steel Targets, Materials, 16(11). DOI: https://doi.org/10.3390/ma16113990.
[10] Andreotti, R., Abate, S., Casaroli, A., Quercia, M., Fossati, R., Boniardi, M. V. (2021). A simplified ale model for finite element simulation of ballistic impacts with bullet splash – development and experimental validation, Frattura ed Integrita Strutturale, 15(57), pp. 223–245. DOI: https://doi.org/10.3221/IGF-ESIS.57.17.
[11] Sonis, P., Reddy, N.V., Lal, G.K. (2003). On multistage deep drawing of axisymmetric components, J Manuf Sci Eng, 125(2), pp. 352–362. DOI: https://doi.org/10.1115/1.1556399.
[12] Ishimaru, E., Takahashi, A., Ono, N. (n.d.). Effect of Material Properties and Forming Conditions on Formability of High-Purity Ferritic Stainless Steel.
[13] Choi, J.-Y., Jin, W. (1997). Strain induced martensite formation and its effect on strain hardening behavior in the cold drawn 304 austenitic stainless steels, 36.
[14] Ishimaru, E., Hamasaki, H., Yoshida, F. (2014). Deformation-induced martensitic transformation and workhardening of type 304 stainless steel sheet during draw-bending., Procedia Engineering, 81, pp. 921–926.
[15] Semiantin, S.L. (2006). ASM Handbook, Volume 14b: Metalworking: Sheet Forming, ASM International.
[16] Wang, L., Lee, T.C. (2006). The effect of yield criteria on the forming limit curve prediction and the deep drawing process simulation, Int J Mach Tools Manuf, 46(9), pp. 988–995. DOI: https://doi.org/10.1016/j.ijmachtools.2005.07.050.
[17] Jaamialahmadi, A., Kadkhodayan, M. (2012). A modified Storen-Rice bifurcation analysis of sheet metal forming limit diagrams, Journal of Applied Mechanics, Transactions ASME, 79(6). DOI: https://doi.org/10.1115/1.4005538.
[18] Paul, S.K. (2013). Theoretical analysis of strain- and stress-based forming limit diagrams, Journal of Strain Analysis for Engineering Design, 48(3), pp. 177–188. DOI: https://doi.org/10.1177/0309324712468524.
[19] Narooei, K., Karimi Taheri, A. (2009). A study on sheet formability by a stretch-forming process using assumed strain FEM, J Eng Math, 65(4), pp. 311–324. DOI: https://doi.org/10.1007/s10665-009-9315-x.
[20] Jagota, V., Preet, A., Sethi, S., Kumar, K. (2013). Finite Element Method: An Overview, 10.
[21] Arasaratnam, P., Sivakumaran, K.S., Tait, M.J. (2011). True Stress-True Strain Models for Structural Steel Elements, ISRN Civil Engineering, pp. 1–11. DOI: https://doi.org/10.5402/2011/656401.
[22] Okayasu, M., Ishida, D. (2019). Effect of Microstructural Characteristics on Mechanical Properties of Austenitic, Ferritic, and γ-α Duplex Stainless Steels, Metall Mater Trans A Phys Metall Mater Sci, 50(3), pp. 1380–1388. DOI: https://doi.org/10.1007/s11661-018-5083-4.
[23] Introduction to ABAQUS. (2009). ABAQUS Analysis User's Manual. Available at: https://classes.engineering.wustl.edu/2009/spring/mase5513/abaqus/docs/v6.6/books/rnb/default.htm?startat=abc11aqs01.html.
[24] Montgomery, D.C. (2013). Design and analysis of experiments, John Wiley & Sons, Inc.
[25] Hwang, D.H., Zum Gahr, K.H. (2003). Transition from static to kinetic friction of unlubricated or oil lubricated steel/steel, steel/ceramic and ceramic/ceramic pairs, Wear, 255(1–6), pp. 365–375. DOI: https://doi.org/10.1016/S0043-1648(03)00063-2.